Spatial and Seasonal Variations of Near-inertial Kinetic Energy in the Upper South China Sea: Role of Synoptic Atmospheric Systems

Juan Li [a, b, c], Xiaoming Zhai [c*], Junliang Liu [a, b], Tong Yan [a, b], Yinghui He [a, b], Zhiwu Chen [a, b], Shuqun Cai [a, b, d, e*]

[a] State Key Laboratory of Tropical Oceanography (South China Sea Institute of Oceanology，Chinese Academy of Sciences), Guangzhou 510301, China

[b] Southern Marine Science and Engineering Guangdong Laboratory (Guangzhou), Guangzhou 511458, China

[c] Centre for Ocean and Atmospheric Sciences, School of Environmental Sciences, University of East Anglia, Norwich, United Kingdom

[d] Institution of South China Sea Ecology and Environmental Engineering, Chinese Academy of Sciences, Guangzhou 510301, China

[e] University of Chinese Academy of Sciences, Beijing, 100049, Chi

Corresponding authors: Shuqun Cai (caisq@scsio.ac.cn), Xiaoming Zhai (xiaoming.zhai@uea.ac.uk)

Keywords: Near-inertial Kinetic Energy; Tropical cyclone; Cold surge; Monsoon; Mixed layer; South China Sea

Abstract

The spatial distribution and seasonal variation of near-inertial kinetic energy (NIKE) in the upper ocean of the South China Sea (SCS) are examined using the Global 1/12° Analysis Hybrid Coordinate Ocean Model and the Navy Coupled Ocean Data Assimilation reanalysis product. The annual mean NIKE in the upper SCS is characterized by a rapid decay with depth and a southwestward decrease from the west of Luzon Island to the southern SCS, reflecting the pattern of near-inertial energy input by the atmospheric wind field. Owing to the changes of near-inertial wind forcing as well as the mixed layer depth, NIKE in the upper SCS exhibits a pronounced seasonal cycle. The magnitude of mixed layer NIKE averaged in the SCS in November-January is found to be approximately twice of that in April-June. Further analysis shows that the variation of near-inertial wind forcing in the SCS can, to a large extent, be explained by northerly cold surges during the winter SCS monsoon and strong tropical cyclones from the Tropical Pacific. In addition, the wind reversal during the monsoon transitional period and the low-level convergence formed by the elevated terrain of islands also contribute to oceanic near-inertial energy in the SCS.

1 Introduction

The South China Sea (SCS) is the largest marginal sea in the western Pacific, with a broad continental shelf and a deep semi-enclosed basin. The SCS has an average depth over 1000 m, and a maximum depth of more than 5000 m. The SCS connects, and exchanges water masses, to the east with the Pacific Ocean through the Luzon Strait (Fig. 1). Owing to its unique geographical location, the SCS is strongly influenced by the monsoon winds and synoptic systems, such as tropical cyclones (TCs), easterly waves, equatorial anticyclones and fronts (Yang et al., 2016).

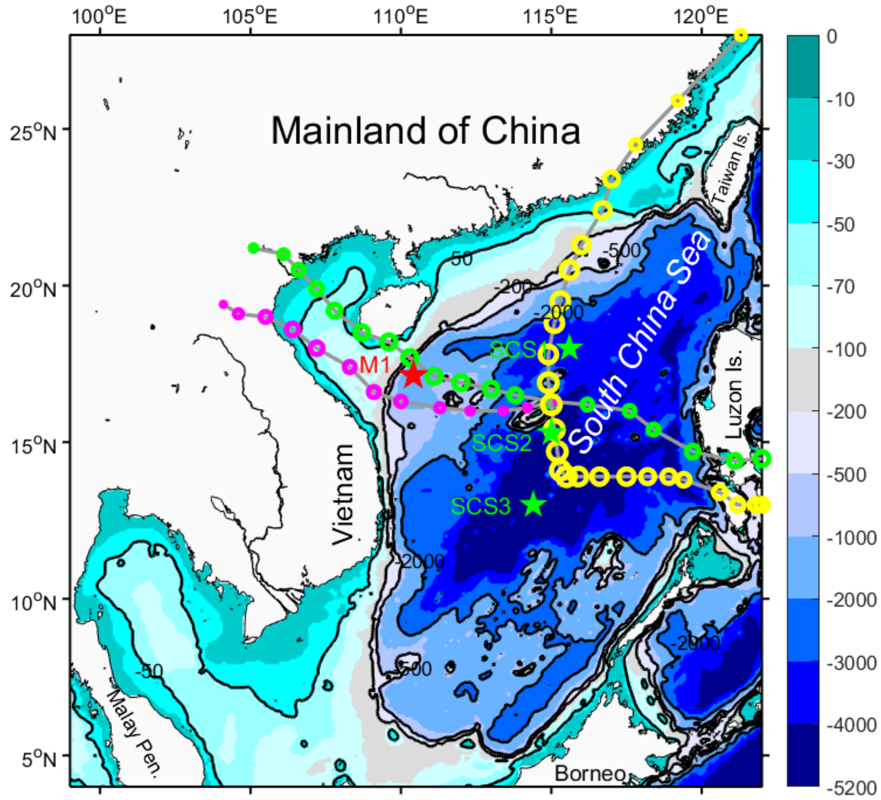

Fig. 1. Bathymetry of the SCS from ETOPO1, with the 50, 200, 500, and 2000 m isobaths labelled. Location of the ADCP mooring station (M1) is marked with red pentagram. The other mooring sites (SCS1, SCS2, SCS3) of ADCPs used in the Appendix are marked with green pentagrams. The tracks of typhoons Conson (July 2010), Mindulle (August 2010) and Chanchu (May 2006) are denoted by green, magenta and yellow circles, respectively. The circle indicates the position of typhoon center every 6 hours, and the size of circle indicates the magnitude of maximum typhoon

speed.

In the SCS, diapycnal mixing plays an important role in determining water mass exchanges between the SCS and the Pacific, and in maintaining the abyssal stratification and meridional overturning circulation (Qu et al., 2006; Zhou et al., 2014; Sun et al., 2016; Xiao et al., 2016). The breaking of internal tides and near-inertial waves are believed to be the major energy sources of diapycnal mixing. In the SCS, internal tides are mainly generated in the Luzon Strait which then travel across the deep basin and propagate southwestward into the southern basin (Xu et al., 2013; Waterhouse et al., 2014; Xu et al., 2016). Wind-induced near-inertial waves are mainly generated by variable wind stress associated with synoptic and mesoscale atmospheric systems such as travelling midlatitude storms, TCs, cold fronts and atmospheric lows. Winter travelling storms at mid-latitudes are responsible for the majority of wind energy input to near-inertial motions in the global ocean (D'Asaro, 1985). The energy flux from atmospheric systems also depends critically on the existence of the background wind field (Dippe et al., 2015; Zhai, 2017). A significant fraction of wind-induced near-inertial waves and the energy they carry appears to be dissipated in the upper 200 m or so, while the rest propagates into the ocean interior, contributing to diapycnal mixing at depths (Zhai et al., 2009).

The SCS is influenced by atmospheric systems spanning a wide range of spatial and time scales. Variability of these atmospheric systems is complex. The SCS monsoon, under the influences of four adjacent monsoon subsystems, is characterized by a distinct seasonal reversal of the prevailing winds lasting for more than 9 months, such as southwesterlies in summer (July-September) and northeasterlies in winter (December-February). There are associated synoptic-scale fluctuations during the prevailing monsoon, such as the cold surges which are accompanied with the onset of the cold front and northerly in the East Asian winter monsoon (Jarvis 1995; Alpers et al., 2012; Abdillah et al., 2021), the TCs and easterly waves from Tropical Pacific, equatorial anticyclones and other synoptic-scale disturbances in the summer season (Zeng et al., 2012; Yang et al., 2016). While the easterly waves and equatorial anticyclones mostly appear in the southern SCS occasionally, the cold surges and TCs always appear in the central and north parts of the SCS.

The occurrence of a cold surge event over the lower troposphere of the SCS is associated with disturbances in mid-latitude atmospheric circulation patterns, which is recognized to be a result of an amplification of the Siberian high and exhibits the characteristics of meso-β-scale (20-200 km) gravity wave and planetary-scale wave. Due to the elevated terrain over Sumatra and southern Peninsular Malaysia which cause low-level convergence, the southward expansion of cold surges sometimes spin up a synoptic-scale cyclonic circulation around the Borneo Island (Kalimantan Island), known as Borneo vortex (Tangang et al., 2008). On average, there are about 9 cold surge events per year or 2 per month and the cold surge event usually lasts for several days during winter monsoon (Chang et al., 2005; Pang and Lu, 2019). The onset of summer monsoon is also observed to excite strong near-inertial currents that are comparable in magnitude to those induced by tropical storms in the central SCS (Shu et al., 2016).

The SCS is frequently visited by the TCs. In the summer of tropical central Pacific Ocean, synoptic lower tropospheric equatorial disturbances tend to propagate northwestward toward the Philippines at roughly 150°E from a packet of mixed Rossby-Gravity waves to individual off-equatorial tropical depression type disturbances, and ultimately intrude into the Asia or the SCS. A small fraction of tropical disturbances can lead to TC formation (Takayabu & Nitta, 1993; Dickinson & Molinari, 2002; Li & Wang, 2005; Wang et al., 2009). TCs with maximum sustained wind speed > 33 m/s are typhoons (Oey & Chou, 2016). On annual average, 10 to 11 TCs pass through the SCS and 3 to 4 TCs originate within the SCS, and the corresponding numbers for typhoons are 6 and 1 to 2, respectively. The TC season is mostly from June to November (Wang et al., 2007). Most previous studies of near-inertial waves in the SCS have focused on observing and modelling the generation of near-inertial motions induced by individual TC and their interaction with the background currents (Sun et al., 2011; Chen et al., 2013; Guan et al., 2014; Sun et al., 2015; Cao et al., 2018; Ding et al., 2018; Hou et al., 2019; Kung et al., 2020). For example, in the northern SCS, during the passage of Typhoon Hagupit, the near-inertial kinetic energy (NIKE) on the continental slope of the northwestern South China Sea was found to be enhanced by a factor of 10, which exceeded the internal tidal energy by a factor of 2 to 3 (Xu et al., 2013). These strong near-inertial motions generated by TCs may last for 1-2 weeks, with current speed reaching over 50 cm/s (Chen et al., 2015). However, the TC-generated near-inertial motions tend to be confined to the tracks of TCs and are also limited by the number of TCs occurring each year. It is, therefore, not clear whether TCs make a significant contribution to the overall near-inertial energy budget in the SCS.

In the past, we applied a simple one-dimensional slab model of Pollard and Millard (1970) to simulate the wind near-inertial energy flux into the mixed layer of the SCS (Li et al., 2015). However, the slab model lacks a damping mechanism that operates on short time scales (Thomas & Zhai, 2022) and does not fully represent the inertial processes, i.e. without near-inertial internal wave wake. In this study, we analyze the realistic high-resolution three-dimentional global simulations to examine near-inertial energy in the upper SCS, and aim to address the following questions: (1) What are the spatial and seasonal distributions of NIKE in the upper SCS? (2) What atmospheric forcing is responsible for such distributions? The paper is organized as follows. Section 2 describes the datasets and analysis methods used in this study. In Section 3, the spatial structure and variability of NIKE in the upper SCS are analyzed. In Section 4, we discuss atmospheric and oceanic processes contributing to the variation of near-inertial energy in the SCS. Finally, conclusions are provided in Section 5.

2 Data and Methods

Estimating basin-wide NIKE distribution in the SCS requires ocean velocities at high temporal (at a resolution of a few hours or less) and spatial resolutions (Klein et al., 2004; Jiang et al., 2005; Rimac et al., 2013), which is not possible with observations. In this study, we use the global 1/12° reanalysis product of the Hybrid Coordinate Ocean Model (HYCOM) and the Navy Coupled Ocean Data Assimilation (NCODA) reanalysis to calculate the near-inertial horizontal kinetic energy, and examine the spatial and variations of NIKE in the SCS. The atmospheric forcing for the global HYCOM reanalysis model comes from the hourly National Centers for Environmental Prediction Climate Forecast System Reanalysis product (CFSR; Saha et al., 2010), which includes surface wind stress, wind speed, heat flux, precipitation and so on. The HYCOM reanalysis product provides sea surface height, water temperature, salinity and two components of ocean velocity every 3 hours on a 1/12.5° global grid. It should be noted that the HYCOM reanalysis involves a complex data assimilation process, and it has no tidal forcing, which excludes parametric subharmonic instability (PSI) and its effect on NIKE.

We apply a band-pass filter with a frequency range of 0.85*f*-1.15*f* (Chen et al., 2013) to the HYCOM velocities in the SCS (4°N-28°N, 98.56°E-122°E) over the period from 1 January 2000 to 31 December 2010. The NIKE is then calculated using

$$\mathrm{NIKE} = \frac{1}{2}\rho_0(u_i^2 + v_i^2), \tag{1}$$

and wind power input to near-inertial motions (WPI) is calculated from

$$\mathrm{WPI} = \boldsymbol{\tau} \cdot \boldsymbol{u}_i, \tag{2}$$

Here ρ_0 =1024 kg m^{-3} is the density of sea water, $\boldsymbol{u}_i$ = (u_i, v_i) is the near-inertial band-pass filtered ocean velocity from HYCOM, and $\boldsymbol{\tau}$ is the unfiltered CFSR surface wind stress.

Wind stress at frequencies close to the local inertial frequency is most effective in exciting near-inertial motions in the ocean (Crawford & Large, 1996; Zhai, 2015). Following Dippe et al. (2015), we define the near-inertial wind stress magnitude (NIWSM) as

$$\mathrm{NIWSM} = \sqrt{\tau_{x,i}^2 + \tau_{y,i}^2}, \tag{3}$$

where $\tau_{x,i}$ and $\tau_{y,i}$ are the near-inertial band-pass filtered CFSR surface zonal and meridional wind stresses.

The wind stress can be calculated from the formula:

$$(\tau_x, \tau_y) = \rho_a C_d \sqrt{u_{10}^2 + v_{10}^2}\,(u_{10}, v_{10}), \tag{4}$$

Where ρ_a =1.3 kg m^{-3} is the air density; $U_{10} = (u_{10}, v_{10})$ is the wind speed at 10 m height above the sea surface provided by the HYCOM Consortium; and C_d is the drag coefficient. Follow Oey et al. (2006), C_d is calculated as (Guan et al., 2014; Cao et al., 2018),

$$C_d = \begin{cases} 1.2 \times 10^{-3}, & U_{10} \le 11m/s \\ (0.49 + 0.065U_{10}) \times 10^{-3}, & 11 < U_{10} \le 19m/s \\ (1.364 + 0.0234U_{10} - 0.0002U_{10}^2) \times 10^{-3}, & 19 < U_{10} \le 100m/s \end{cases},$$

(5)

which fits the formula proposed by Large and Pond (1981) for low-to-moderate wind speeds and by Powell et al. (2003) for high wind speeds.

The cold surge index is constructed using the 925-hPa meridional wind averaged between 110°E and 117.5°E along 15°N. A cold surge event occurs when this index exceeds 8 m/s (Chang et al. 2005). The latest climate reanalysis ERA5 data produced by European Centre for Medium-Range Weather Forecasts (ECMWF) are used to calculate the 925-hPa wind velocities and surface air temperature (SAT) anomalies. The bathymetry is taken from ETOPO1 (Amante and Eakins 2009). The 6-hourly best-track TC data are obtained from the Joint Typhoon Warning Center (JTWC), which provides the location of the TC center, maximum sustained 10-m height wind speed and the radius of maximum wind.

The mixed layer depth (MLD) is defined as the depth where the water temperature is lower than the sea surface temperature (SST) by 0.5°C, following Monterey et al. (1997). The observed current velocity profile comes from an up-looking and a down-looking RDI Workhorse Long Ranger 75-Khz Acoustic Doppler Current Profiler (ADCP) moored at location M1 (approximately 17.10°N, 110.39°E) near Xisha Island of the northwestern SCS (Fig. 1). The time series data from 4 July 2010 to 4 September 2010 with a depth interval of 8 m and a sampling time interval of 1 hour are used here (Chen et al., 2013; Yang et al., 2015; Zeng et al., 2015; Liu et al., 2018). The measurements were taken in the upper 450 m, and due to measurement errors, the recording in the upper 50 m is less reliable.

3 Spatial and temporal variations of near-inertial kinetic energy

3.1 Comparison of HYCOM reanalysis data with observations

Figure 2 displays the time series of near-inertial currents observed at the mooring station M1 and near-inertial currents (17.12°N, 110.4°E) simulated by HYCOM in the upper 200 m from 4 July 2010 to 4 September 2010. Typhoon Conson (Fig. 1) passed through the mooring station on 16 July 2010, and typhoon Mindulle (Fig. 1) travelled on the left side of mooring station on around 23 August 2010. The observed depth range (Fig. 2a and Fig. 2c) is from -13 m to -205 m with a vertical resolution of 8 m, and the HYCOM depth range (Fig. 2b and Fig. 2d) is from 0 m to 200 m with 14 unequal vertical layers.

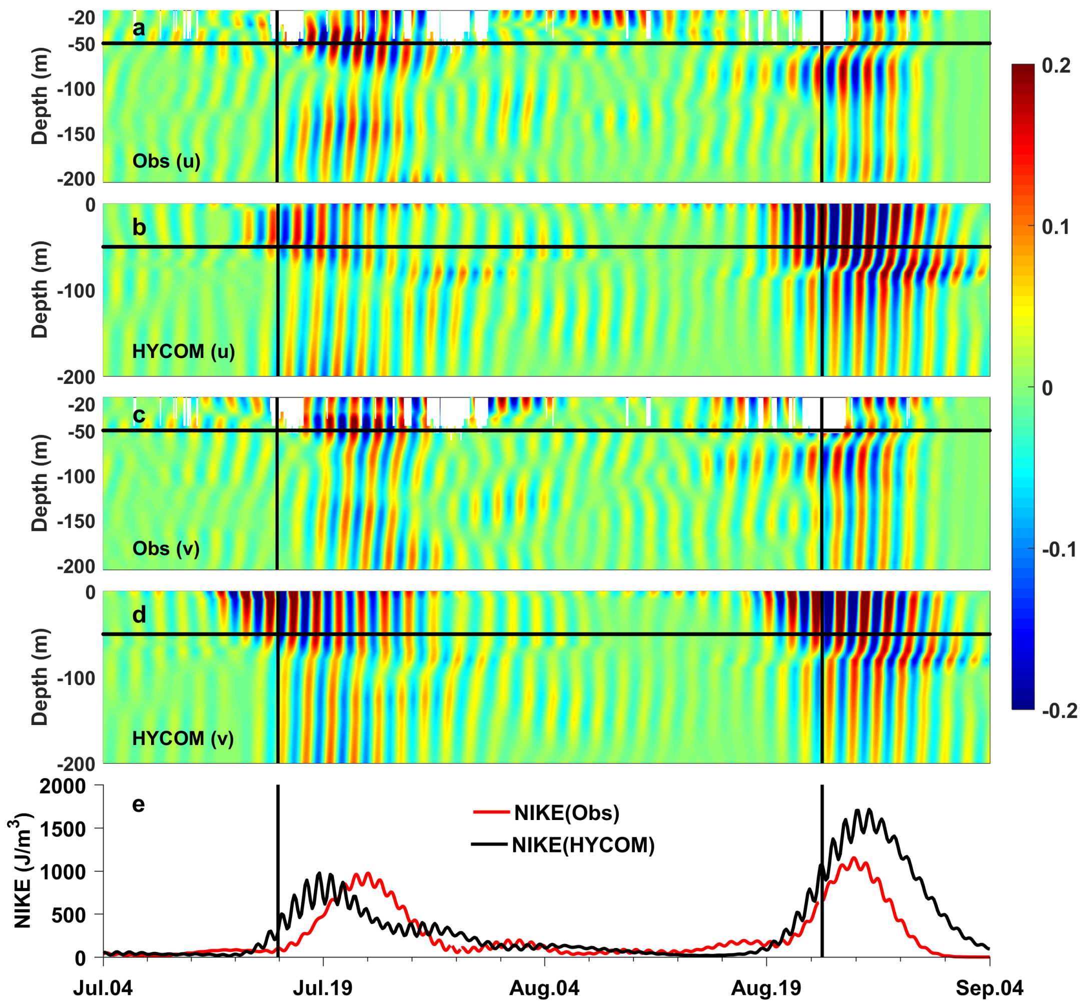

Fig. 2. Time series of the eastward and northward components of (a, c) observed near-inertial currents (m/s) and (b, d) HYCOM-simulated near-inertial currents (m/s) in the upper 200 m from 4 July 2010 to 4 September 2010. (e) Depth-integrated (-50 m to ~-200 m) observed NIKE (red line, J/m^3) and HYCOM-simulated NIKE (black line). The horizontal black lines in (a-d) mark the

50 m depth. The vertical black lines denote the time when the centers of typhoon Conson and Mindulle are nearest to the mooring.

There is a reasonable agreement between the observed near-inertial currents (Fig. 2a; Fig. 2c) and the HYCOM-simulated near-inertial currents (Fig. 2b; Fig. 2d). The maxima of the observed near-inertial currents and the HYCOM near-inertial currents are 0.32 m/s and 0.33m/s at 20 m depth, 0.26 m/s and 0.26 m/s at 50 m depth, 0.16 m/s and 0.17 m/s at 100 m depth, respectively. Figure 2e displays the depth-integrated (from -50 m to ~-200 m) observed NIKE (red line) and HYCOM-simulated NIKE (black line). Both typhoon Conson and Mindulle trigger significantly increased NIKE. The magnitude of typhoon Conson-induced NIKE (former) simulated by HYCOM generally agrees with that of observations, while the HYCOM-simulated NIKE during typhoon Mindulle (latter) is larger than the observed NIKE. The correlation coefficient between the depth-integrated observed NIKE and HYCOM-simulated NIKE reaches 0.82 (significant at the 0.01 level).

Furthermore, the profiles of time-averaged observed near-inertial currents (red circles) and the HYCOM-simulated near-inertial currents (black circles) are shown in Fig. 3. The currents exhibit a good agreement at depths greater than 50 m, but the magnitude of HYCOM-simulated near-inertial currents is slightly larger than that of the observations. More observed near-inertial currents, for example, at locations of SCS1, SCS2 and SCS3, are compared with the HYCOM-simulated near-inertial currents (Fig. S1 in the Appendix). The variability of HYCOM near-inertial currents is found to be broadly consistent with that of the observations. HYCOM simulations have also been used previously to study the influence of mesoscale eddies on the near-inertial waves and the typhoon-induced near-inertial waves (Cao et al., 2021; Yang et al., 2021).

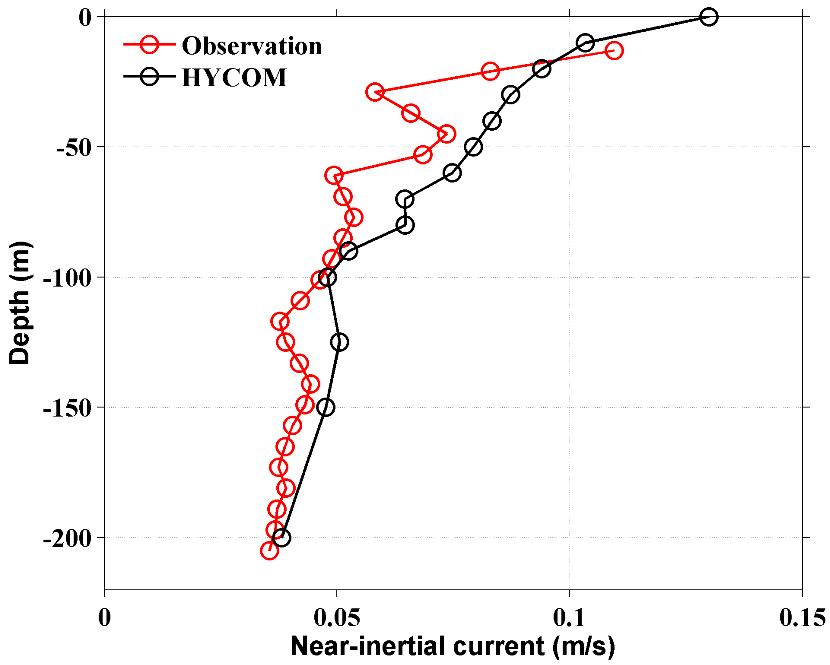

Fig. 3. Profiles of time-averaged observed near-inertial currents (red circles, m/s) and HYCOM-simulated near-inertial currents (black circles, m/s) in the upper ocean from 4 July 2010 to 4 September 2010.

3.2 Annual mean

The spatial distribution of time-mean NIKE in the upper 200 m of the SCS over the period of 2000-2010 is shown in Fig. 4. The magnitude of surface NIKE decreases southwestward from as large as 9 J/m^3 to the west of Luzon Island to about 4-5 J/m^3 in the central SCS. A similar pattern of southwestward decrease in NIKE is seen throughout the upper 200 m. Most of the NIKE in the SCS is confined in the deep water; the level of NIKE on the continental shelf and close to the coast is generally very low. The small amplitude of NIKE in shallow coastal regions has been attributed to dissipation and energy transfer out of near-inertial oscillations into other wave motions such as seiches (Anderson et al., 1983; Chen et al., 1996; Hisaki & Naruke, 2003; Chen et al., 2017).

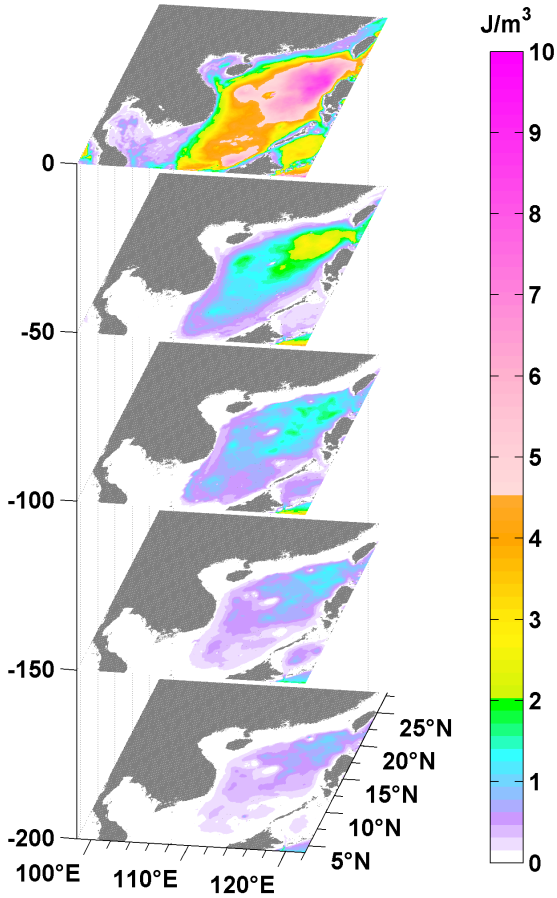

Fig. 4. Spatial distribution of time-mean NIKE (J/m^3) in the upper 200 m of the SCS over the period of 2000-2010.

The magnitude of NIKE decays rapidly with depth, especially in the upper 100 m (Fig. 5). The area-averaged NIKE in the SCS is about 2.6 J/m^3 at the sea surface, whereas it is less than 0.15 J/m^3 at 500 m depth. Further analysis shows that about 29%, 73% and 87% of NIKE in the HYCOM reanalysis model is lost within the upper 50 m, 100 m and 200 m, respectively, with less than 10% of the surface NIKE propagating into the deep SCS below 500 m. This result is broadly consistent with the findings of previous studies in the global average records (Furuichi et al., 2008; Zhai et al., 2009), that is, the majority of the wind-generated NIKE is dissipated within the surface mixed layer and only approximately 10-20% of the NIKE injected at the surface is able to propagate into the ocean interior in the SCS.

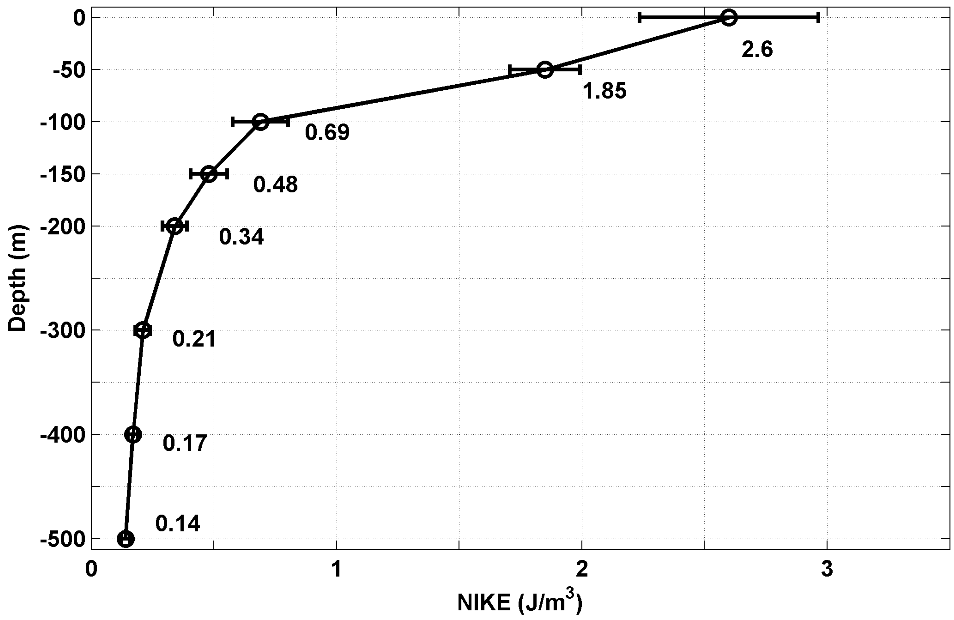

Fig. 5. Time-mean NIKE (J/m^3) averaged horizontally in the SCS over 2000-2010. The numbers indicate the area-averaged NIKE at each depth. Error bars represents one the standard deviation of the average.

To understand the spatial pattern of time-mean NIKE in the SCS, we compute the time-mean near-inertial WPI. Figure 6 shows that large WPI is generally found over the deep basin of the SCS and that the magnitude of WPI decreases from Taiwan and Luzon Island southwestward in a way similar to that of the time-mean NIKE in the upper SCS (Fig. 4). Furthermore, high values of WPI and surface NIKE are both found in a small area close to the west of Luzon Island. Therefore, to a large extent, the spatial distribution of time-mean NIKE in the upper SCS can be explained by the pattern of near-inertial energy input by the atmosphere wind field.

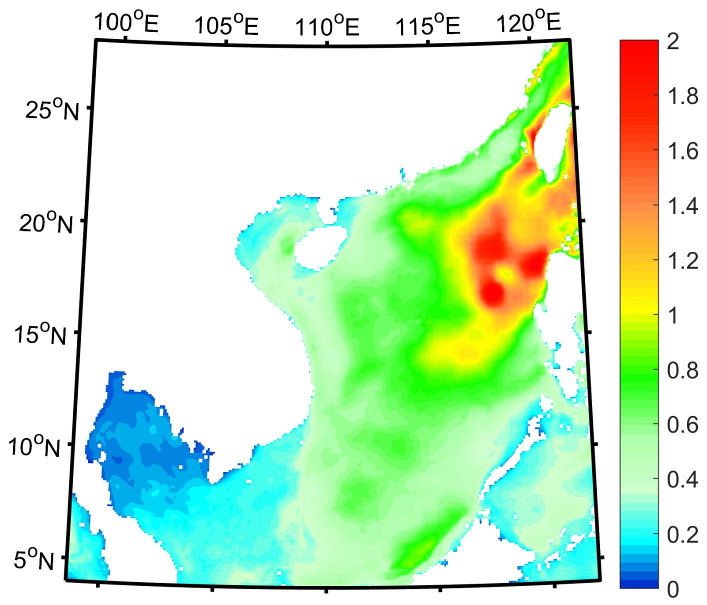

Fig. 6. Time-mean WPI (mW/m^2) to surface SCS over 2000-2010.

3.3 Seasonal variation

Figure 7 shows the climatological monthly mean surface NIKE. The surface NIKE shows large areas of high values, especially in May, July, November and December. After analyzing the surface NIKE month by month, the large NIKE in May and July can be attributed to some strong TCs, e.g., typhoon Chanchu in May 2006 (see Fig. 1). After manually removing the TC-induced NIKE, i.e. excluding the NIKE in the SCS from the appearance of evident TC-induced NIKE to its disappearance, there shows considerable seasonal variations in the magnitude and pattern of surface NIKE in the SCS (Fig. 8). From October to March, a patch of high values of surface NIKE is found to the west of Luzon Island, with a magnitude exceeding 7 J/m^3. This patch of large surface NIKE gradually disappears over the rest of the year. There is a second local maximum to the north of Borneo during summer and autumn (June-November), most pronounced in November.

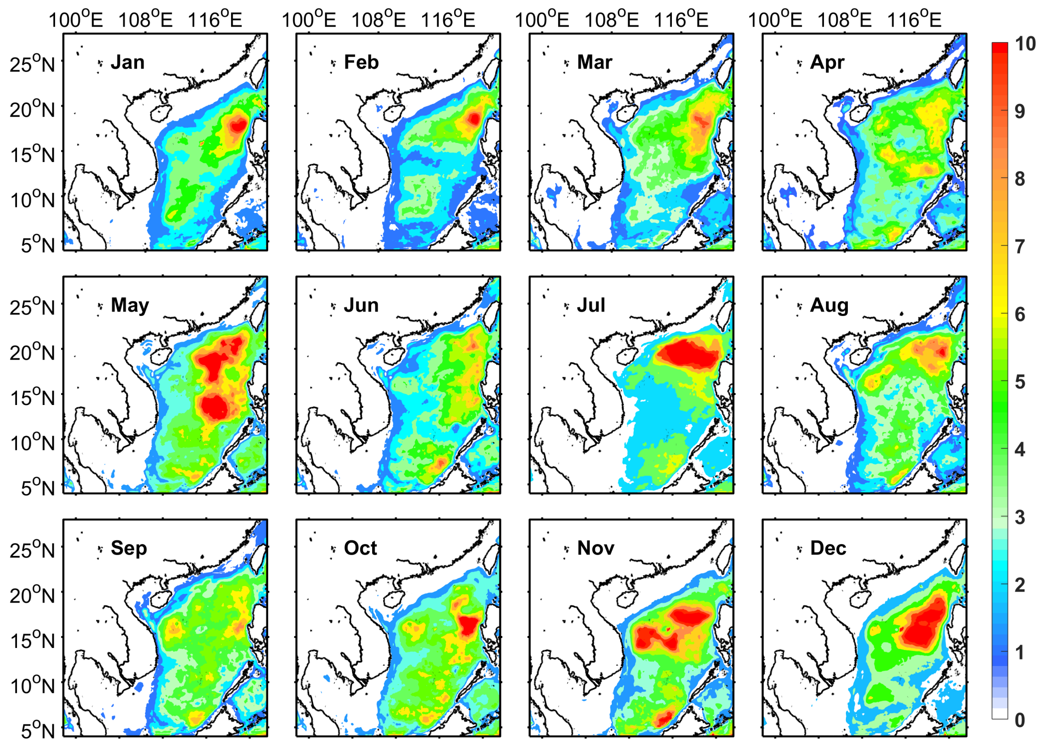

Fig. 7. Climatological monthly mean surface NIKE (J/m^3) in the SCS over the period of 2000-2010.

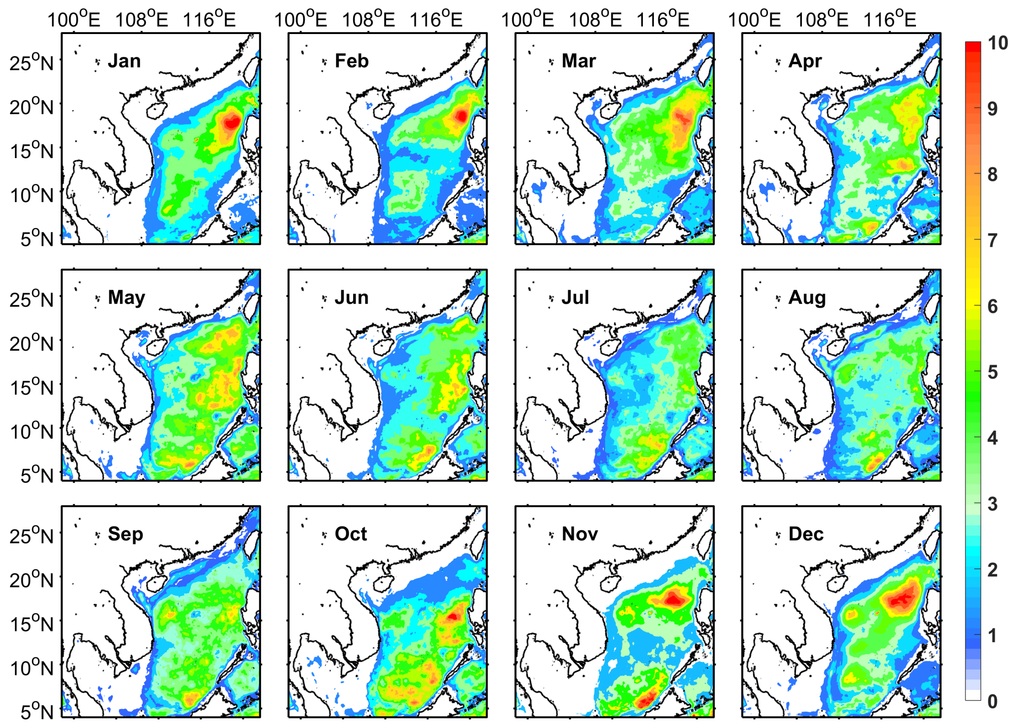

Fig. 8. Climatological monthly mean surface NIKE (J/m^3) in the SCS over the period of 2000-2010

after removing the TC-induced NIKE.

The climatological monthly mean of WPI after removing the TC-induced WPI in the SCS over the 11-year study period is shown in Figure 9. The WPI has large values in the northeast SCS from October to March but only modest values over the rest of the year. Large values of WPI are more widespread in December, extending into the central SCS. There is also a hint of elevated WPI to the north of Borneo in October and November. Several features found in the seasonal distribution of WPI are consistent with those noted in the surface NIKE (Fig. 8). On the other hand, the magnitude of WPI in May is relatively small and is not so different from those in the following summer months, which is at odds with the large surface NIKE found in May (Fig. 8). It is supposed to be due to the weak wind field during the transition period of monsoon.

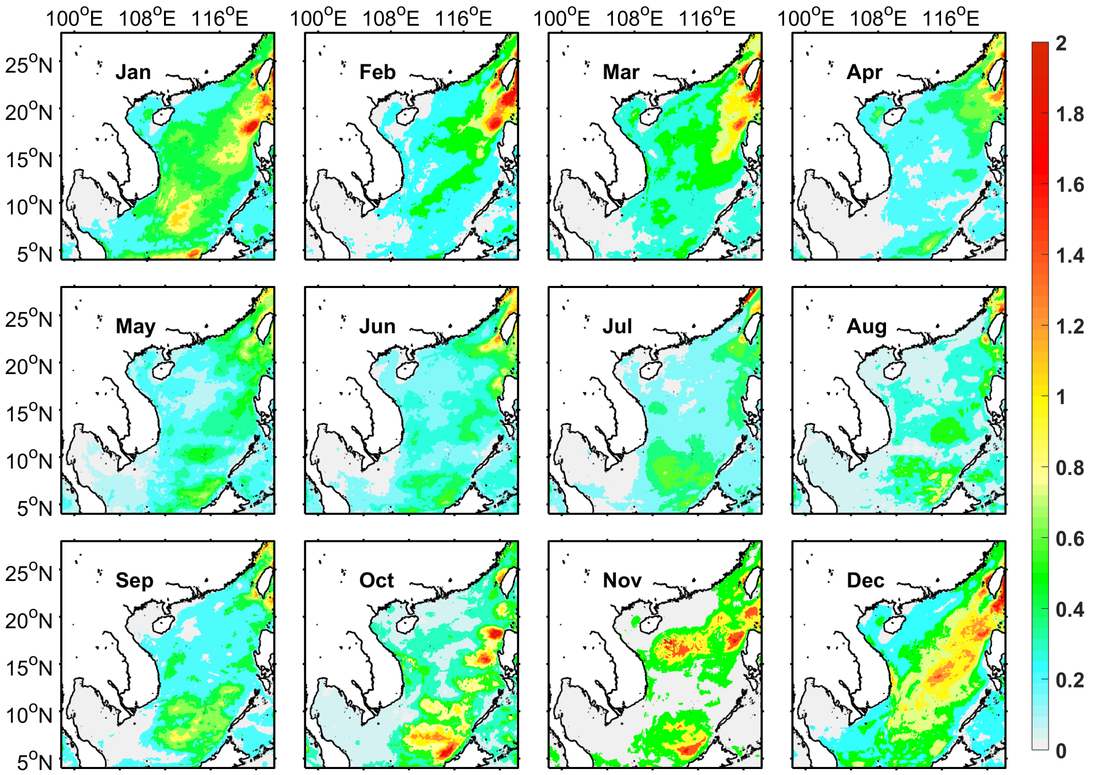

Fig. 9. Climatological monthly mean WPI (mW/m^2) to surface SCS over the period of 2000-2010 after removing the TC-induced WPI.

4 Mechanism for distributions of NIKE and WPI

4.1 Near-inertial wind stress

To understand the seasonal variation of WPI in the SCS, we calculate the magnitude of near-inertial wind stress in each month. In order to remove the influence of TCs efficiently, the TC-related NIWSM is also manually removed and the result is shown in Fig. 10. Recall that near-inertial wind stress is the most efficient atmospheric wind forcing in exciting near-inertial currents in the ocean (Crawford & Large, 1996; Dippe et al., 2015; Zhai, 2015). The climatological monthly mean of NIWSM exhibits large values around the Luzon Strait from November to March. These large values of NIWSM stretch southwestward across the SCS from November to January, resulting a second NIWSM maximum next to the Vietnam coast. The basin-wide NIWSM decreases in magnitude from February, reaching minimum in April before gradually increasing after that. Overall, the seasonal variation of NIWSM in the SCS is mostly consistent with that of WPI, demonstrating that NIWSM is indeed a useful atmospheric proxy for estimating variability of WPI (Rath et al., 2014; Dippe et al., 2015).

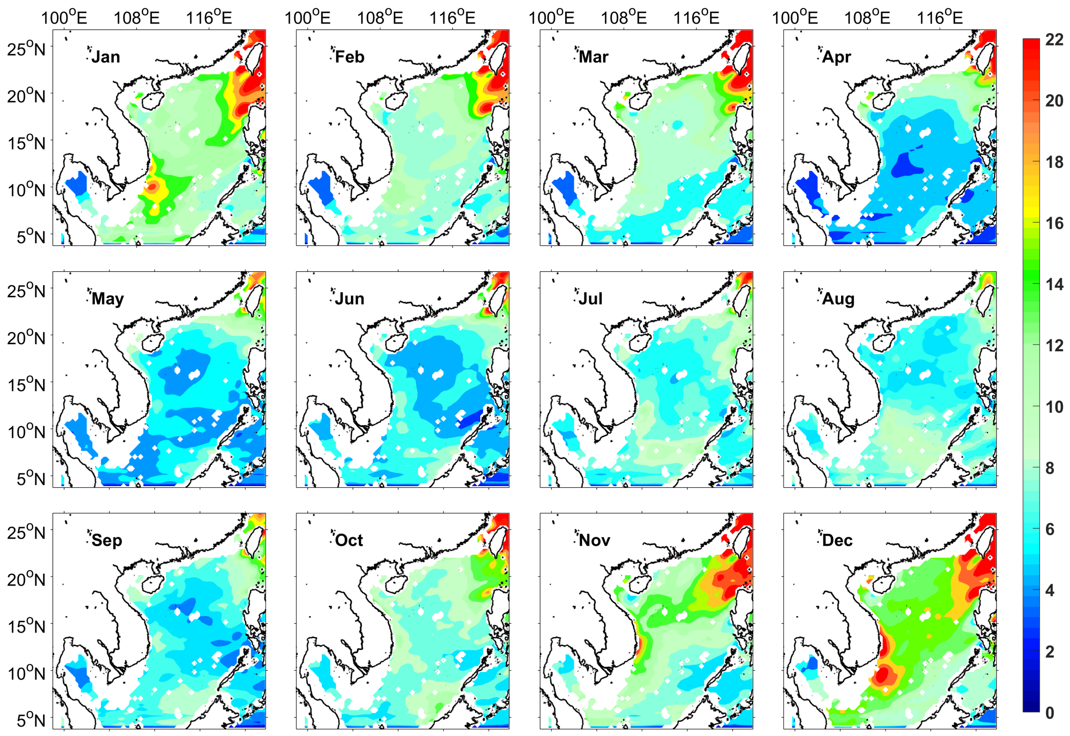

Fig. 10. Climatological monthly mean NIWSM (10^{-3} N/m^2) in the SCS over the period of 2000-2010 after removing the TC-related NIWSM. Regions shallower than 50 m are excluded

in the calculation.

4.2 Mixed layer depth

Although seasonal variations of NIWSM and WPI explain a number of features seen in the seasonal distribution of surface NIKE, there are a few mismatches. For example, the patch of large surface NIKE in November-March is found to the west of Luzon Island, whereas high values of WPI and NIWSM is centered further northeast into the Luzon Strait. The mismatch between NIWSM and surface NIKE shows that ocean properties, in particular the MLD, play a role in determining the pattern of surface NIKE. Using a slab model, Rath et al. (2014) derived the following relationship between WPI, surface NIKE and MLD:

$$\frac{\overline{NIKE}}{\overline{WPI}} = \frac{1}{2\varepsilon H}, \tag{6}$$

where H is the MLD, $1/\varepsilon$ is a linear damping time scale that is usually set to be 2-10 days, and overbar represents a monthly mean. Equation (6) shows that the magnitude of surface NIKE is inversely proportional to the MLD, i.e., the larger the MLD, the smaller the surface NIKE.

Figure 11 shows the climatological monthly mean MLD in the SCS over 2000-2010. The MLD is generally found to be shallow in spring/summer and deep in autumn/winter, especially in the northern SCS, similar as shown in previous studies (Xiao et al., 2013). A particular noticeable feature in Fig. 11 is an area of small MLD to the west of Luzon Island from November to March, coinciding with the west Luzon Cold Eddy (Qu et al., 2000; He et al., 2015). This minimum MLD to the west of Luzon Island confines the near-inertial energy in a thin surface mixed layer and as such results in large values of surface NIKE found there. Similarly, the second maximum of surface NIKE off Borneo in November is likely due to a combination of the synoptic scale convective system (so-called Borneo vortex) and the small MLD there.

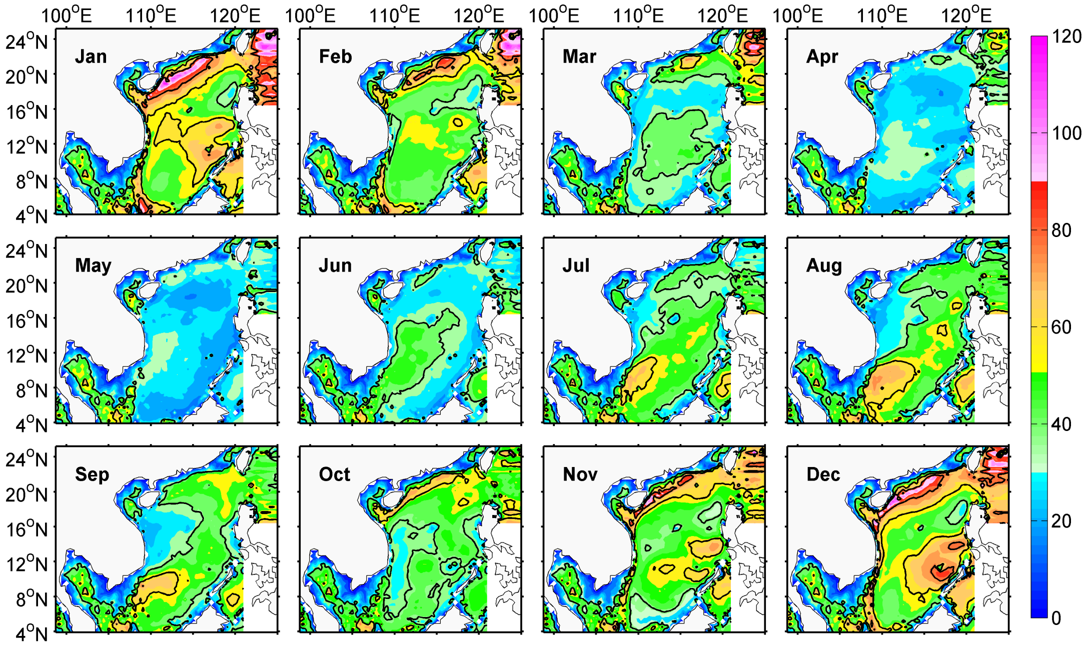

Fig. 11. Climatological monthly mean MLD (m) in the SCS over the period of 2000-2010.

Rearranging Eq. (6), we get

$$\frac{\overline{NIKE}*H}{\overline{WPI}} = \frac{1}{2\varepsilon} \,, \tag{7}$$

which means that the distribution of NIKE integrated over the surface mixed layer mirrors that of the WPI more closely, if we assume that spatial variations of the damping time scale are small. Figure 12 shows that although the hot spot of mixed-layer-integrated NIKE is still located to the west of Luzon Island in November-March, the high values now extend further northeast into the Luzon Strait. As such, the spatial pattern of mixed-layer-integrated NIKE more closely resembles that of WPI than surface NIKE. Further discrepancies in the spatial distributions of mixed-layer-integrated NIKE and WPI in the northeast SCS may be associated with spatially varying ε and interaction of near-inertial waves with mesoscale currents (Lian et al., 2015; Gao et al., 2019; Le Boyer et al., 2020; Chu et al., 2020) that are not accounted for in (7). These results highlight the role of the MLD in the distribution of the NIKE in the upper layer of the SCS.

Averaged horizontally over the SCS (including the influence of TCs), NIWSM, WPI and mixed-layer-integrated NIKE share a similar pattern of pronounced seasonal cycle (Fig. 13), with values in November-January approximately twice of those in April-June. In contrast, the surface NIKE shows a very different seasonal cycle that peaks in May with little variations in the second half of the year.

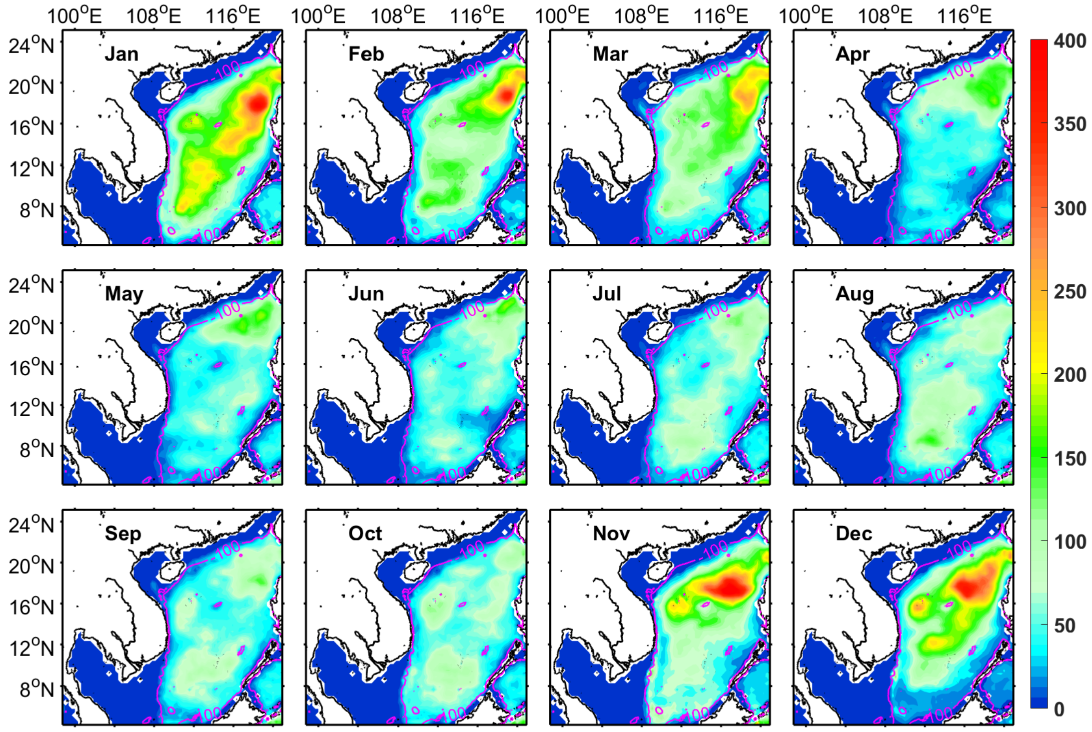

Fig. 12. Climatological monthly mean NIKE (J/m^2) integrated over the mixed layer in the SCS after removing the TC-induced NIKE. The Magenta lines indicate the 100 m isobaths.

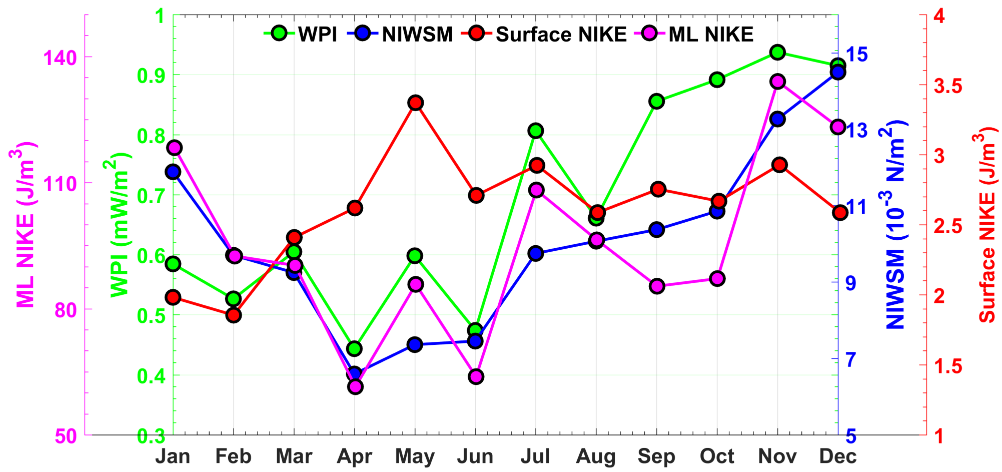

Fig. 13. Monthly-mean WPI (green), NIWSM (blue), surface NIKE (red) and mixed-layer-integrated NIKE (magenta) averaged horizontally in the SCS. Regions shallower than

100 m are excluded in the calculation.

4.3 Synoptic activities in the SCS

Our results demonstrate that the magnitude and pattern of near-inertial wind stress, to the leading order, determine the spatial structure and variation of NIKE in the upper SCS. As shown in Fig. 10, NIWSM displays large values in regions close to Taiwan and the Luzon Strait over most time of the year and there appears to be a band of elevated NIWSM intruding into the southern SCS from November to January. In this section, we discuss processes contributing to the near-inertial wind forcing and the NIKE in the SCS.

As noted in the introduction, synoptic storms and weather systems are responsible for the majority of NIWSM and WPI to the global ocean. Following Dippe et al. (2015), we apply a band-pass filter to the 10-m NCEP/CFSR wind field to isolate synoptic-scale wind variability on timescales of 2-6 days. Figure 14 displays a pronounced seasonal cycle of synoptic atmospheric variability in the Northwest Pacific. In winter, the mid latitude synoptic atmospheric activities tend to be more intense and more frequent, and spreads equatorward intruding the northern SCS. According to the previous studies, synoptic-scale wind events that are particularly important for the SCS during the East Asian winter monsoon (November-March) is the outbreak of cold surges characterized by strong northerly winds originating from the mid-latitude region.

Whereas in summer, there appears to be a band of elevated synoptic storm activities that tilts northwestward stretching from the equator to the northern and central SCS. It is well known that TCs, mostly originated in the tropical Pacific, are active in the summer of SCS, which can excite strong near-inertial waves. Figure 15 shows the spatial statistics of TC tracks in the SCS with wind speed greater than 24 m/s during the period of January 2000 to December 2010 based on the JTWC best-track data. There are no less than 80 TCs passing through the SCS or originating in the SCS, including 28 typhoons and 10 super typhoons. The northeastern SCS, e.g., west of Luzon Strait and Luzon Island, is a region where TCs visit most frequently. So the underlying atmospheric process may be associated with the westward propagations of TCs or tropical disturbances. In order to prove this hypothesis, a series of analyses are conducted as follows.

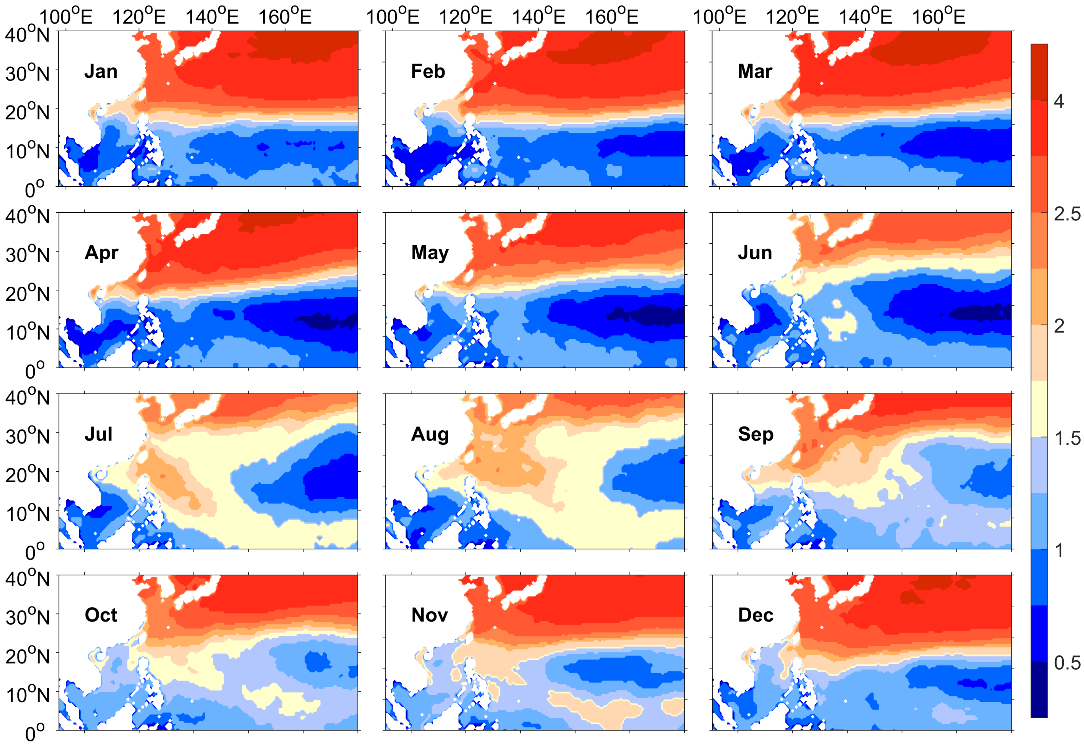

Fig. 14. Climatological monthly mean synoptic-scale wind variability (m/s) in the Northwest Pacific over the period of 2000-2010.

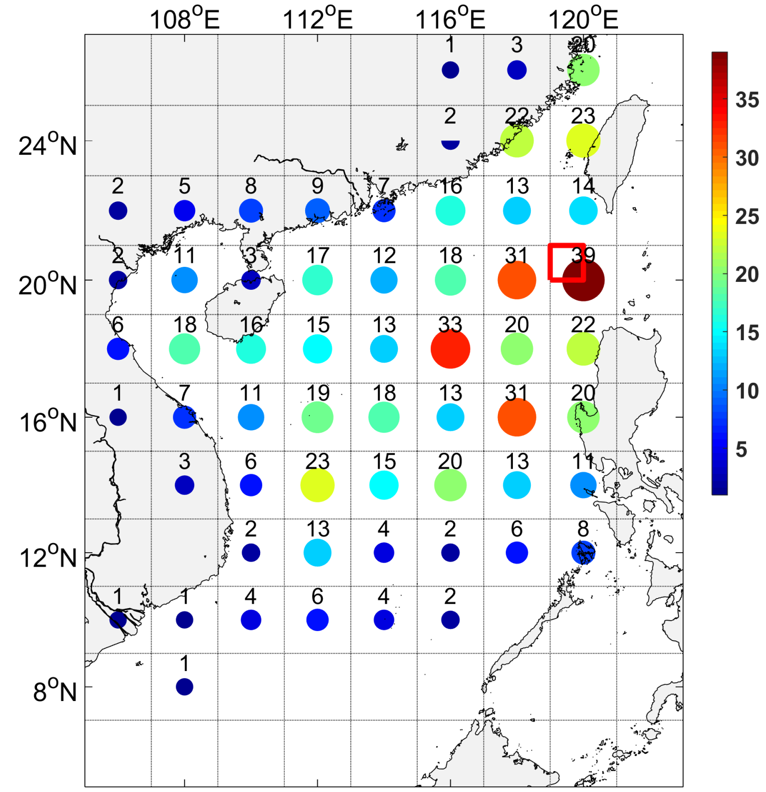

Fig. 15. Distribution (color spotted) of TCs' passages over the period of January 2000 to December 2010 based on the JTWC best-track data. TC tracks with wind speed greater than 24 m/s are counted in each grid box. The red square box (20°N-21°N, 119°E-120°E) indicates the study area shown in Fig. 17.

The NIKE during a typical cold surge event and an occurrence of TC is investigated in Fig.16. During the period from 1 to 7 November 2002, the 925-hPa wind field gradually moves southward from the north，and the surface air temperature (SAT) drops associated with that (Figs. 16a-d). The cold surge index exceeds 8 m/s from 3 November to 5 November, which indicates the occurrence of a cold surge event. The corresponding mixed-layer-integrated NIKE shows significant enhancement during the cold surge event in the northern SCS (Figs. 16e-h). Figures 16i-p show that when strong TC Krovanh passes over the northern SCS from 22 to 26 August 2003, it results in SST cooling and generates large NIKE in its wake (Figs. 16m-p). This case study shows that both cold surges and strong TCs are important in generating enhanced NIKE in the SCS.

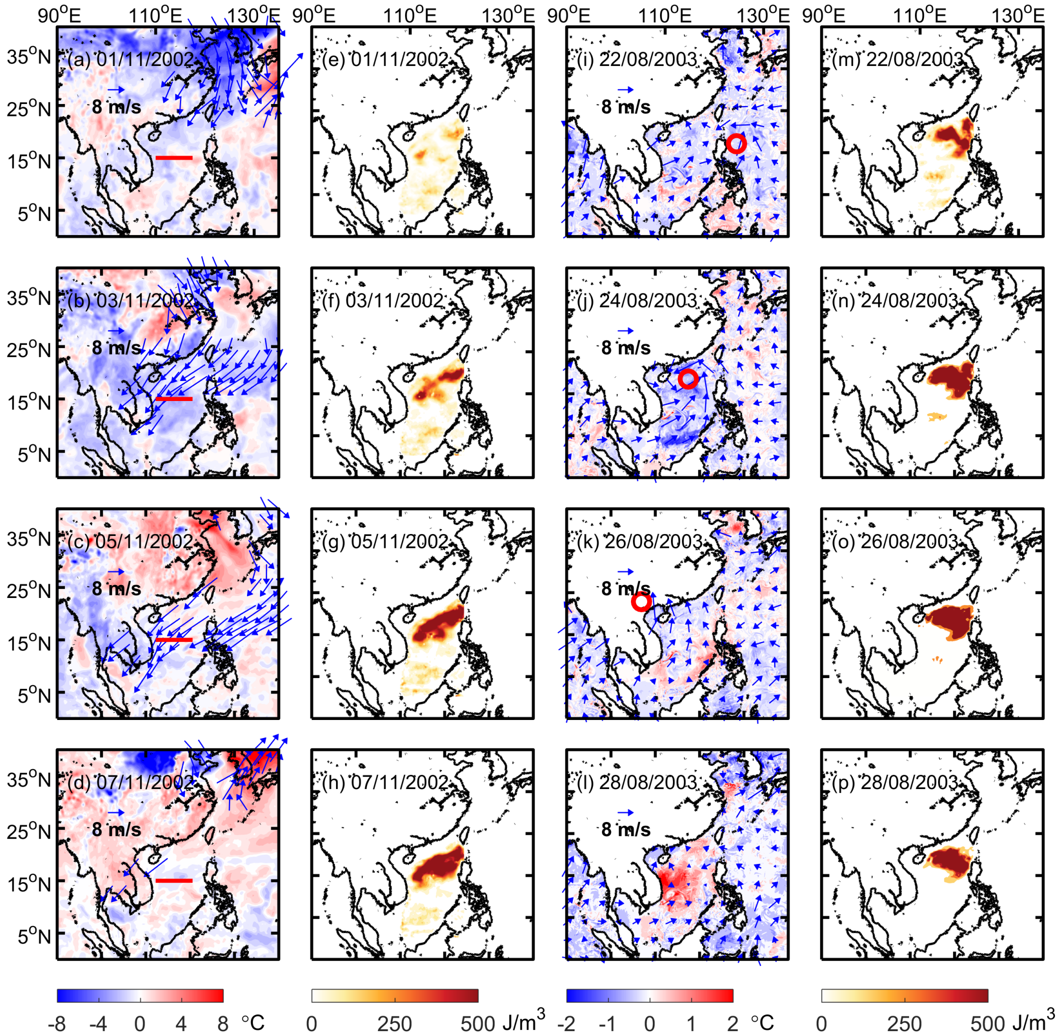

Fig. 16. Maps of (a-d) SAT anomalies (°C; shading) and 925-hPa wind velocities (m/s; vectors) every two days during the period from 1 to 7 November 2002 from ERA5 data. Here only significant wind vectors (meridional wind speed larger than 8 m/s) are drawn and the red lines denote the longitudes 110°E-117.5°E along 15°N. (e-h) The corresponding distributions of mixed-layer-integrated NIKE (J/m^3). (i-l) SST anomalies (°C; shading) and wind velocities (m/s; vectors) at 10 m height above the sea surface every two days during the period of 22 to 28 August 2003. The red circles indicate the positions of the strong TC (Krovanh) centers. (m-p) The corresponding distributions of mixed-layer-integrated NIKE (J/m^3). Here SAT anomalies and SST anomalies are defined as the temperatures differences compared with 24 hours before.

To further investigate the impact of cold surges and TCs on the variations of NIKE in the SCS, one of the most influenced areas enclosed by the red box shown in Fig. 15 (Sun et al., 2017) is studied here for the period from 1 January 2002 to 31

December 2003. The strongly varying wind stress reflects the seasonally reversing wind in monsoon seasons and strong wind associated with the TCs (Fig. 17a). The positive synoptic wind anomaly (Fig. 17b) usually indicates the occurrence of a synoptic or mesoscale atmospheric event, such as the passage of a TC, and it shows that the synoptic atmospheric events occur more frequently during the winter monsoon. Figure 17c displays the cold surge index (gray solid line) and the outbreaks of cold surges (red lines). There are on average one or two cold surge events occurring per month from October to March which are in agreement with previous studies. The corresponding time series of NIWSM and WPI (Figs. 17d, e) show that the enhancement of NIWSM and WPI during the winter monsoon season is typically aligned with the onset of cold surges. NIWSM, WPI and mixed-layer-integrated NIKE (black lines in Figs. 17d, e, and f) are significantly correlated, with the correlation coefficient between NIWSM and mixed-layer-integrated NIKE being 0.60, significant at the 0.01 level.

In the small red box region, the mixed-layer-integrated NIKE (Fig. 17f, black line) shows a sharp increase when typhoon Imbudo (Magenta dashed line) passes through in July 2003. Typhoon Noguri excites a second peak in June 2002, while the other TCs passing through this area fail to trigger significant NIKE, which may be attributed to the difference of TCs characteristics (Sun et al., 2015; Cao et al., 2018; Li et al., 2019; Zhang et al., 2021) such as TC intensity, translation speed and spatial scale. During the winter monsoon, a cluster of enhanced NIKE is usually excited with the onset of cold surges. During the period from 1 January 2002 to 31 December 2003, about 30% of the total mixed-layer time-integrated NIKE (Fig. 17g, black line) in the red box region is excited by the TCs and about 40% is excited by cold surges. Similar percentages are also found for the whole SCS region (Fig. 17g, green line), demonstrating that TCs and cold surges are the major drivers of NIKE in the upper ocean of the SCS. During the transition of seasonal monsoons, the reversal of wind direction (e.g., in the spring of 2003) also trigger a moderate level of near-inertial energy.

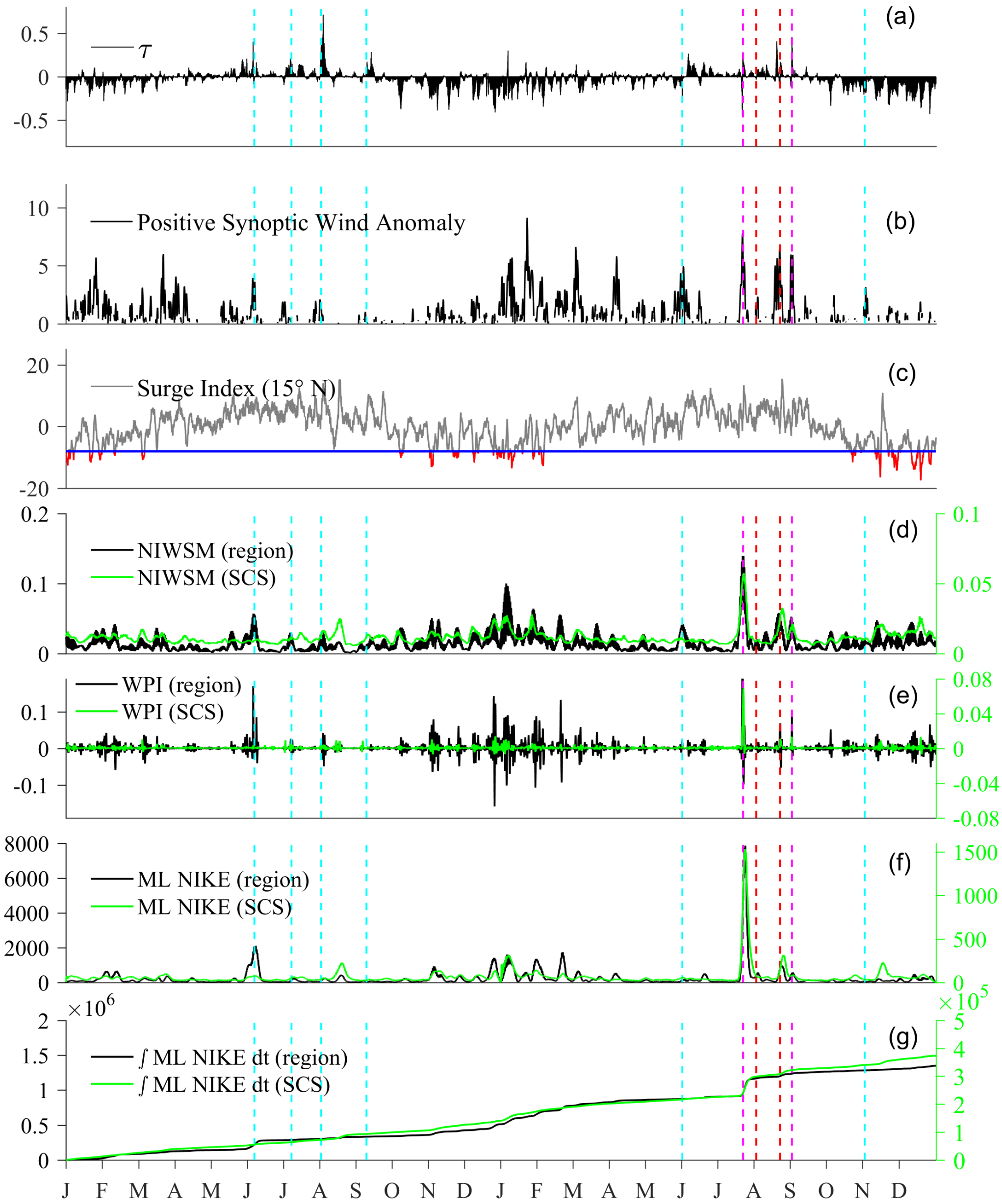

Fig. 17. Time series of (a) wind stress (N/m^2), (b) positive synoptic wind anomaly (m/s) and (c) cold surge index (gray solid line) averaged over the red box area shown in Figure 15 during the period from 1 January 2002 to 31 December 2003. In (c), the blue line marks 8 m/s and the occurrence of cold surges is marked by red lines. (d) NIWSM (N/m^2), (e) WPI (W/m^2), (f) mixed-layer-integrated NIKE (J/m^3) and (g) mixed-layer time-integrated NIKE (J/m^3) averaged over the red box area (black) and over the whole SCS (green) during the same time period. Magenta, red, cyan dashed lines indicate the arrivals of strong TCs (Imbudo in July 2003 and Dujuan in September 2003), moderate TCs (Morakot and Krovanh in August 2003) and the other

weaker TCs around the red box area, respectively.

Overall, our analyses show that the variability of NIWSM (and hence NIKE) in the SCS can, to a large extent, be explained by a combination of seasonal intrusions of cold surges from the temperate zone in boreal winter, and TCs from tropical Pacific in boreal summer and autumn.

5 Concluding remarks

In this study we have investigated the spatial distribution and seasonal variation of NIKE in the upper SCS using the high-resolution global HYCOM reanalysis output. The main findings are as follows:

- The spatial distribution of time-mean NIKE in the upper SCS is characterized by a southwestward decrease from the west of Luzon Island to the central and southern SCS, which largely reflects the pattern of near-inertial energy input by the atmospheric wind field.
- The magnitude of NIKE decays rapidly with depth, especially in the upper 100 m. Over 85% of NIKE is lost to dissipation within the upper 200 m, with less than 10% of the NIKE injected at the surface propagating into the deep SCS below 500 m.
- Owing to seasonal changes of NIWSM and MLD, NIKE in the upper SCS exhibits a pronounced seasonal cycle. The magnitudes of SCS-averaged NIWSM, WPI and mixed layer NIKE in November-January are approximately twice of those in April-June.
- An area of large NIKE is found to the west of Luzon Island from November to April, coinciding with the West Luzon Cold Eddy. This hot spot of NIKE results from a combination of large NIWSM and small MLD in these months.
- The variability of NIWSM (and hence WPI and NIKE) in the SCS can, to a large extent, be explained by the intrusion of cold surges from the north during East Asian winter monsoon, and TCs from tropical Pacific in boreal summer and autumn months. These two atmospheric systems contribute to near 70% of the near-inertial energy budget in the upper SCS.

Acknowledgments

This work is jointly supported by National Natural Science Foundation of China Grants 42130404, 41890851 and 42176025, Grant No. GML2019ZD0304 from Southern Marine Science and Engineering Guangdong Laboratory (Guangzhou), the Key Research Program of Frontier Sciences, Chinese Academy of Sciences (CAS) (No. QYZDJ-SSW-DQC034), No. ISEE2021PY01 from CAS, Youth Innovation Promotion Association CAS (2019336), and the State Key Laboratory of Tropical Oceanography Independent Research Program under contract No. LTOZZ2205. Juan Li is supported by the China Scholarship Council to visit the University of East Anglia. The 1/12 deg global HYCOM+NCODA Ocean Reanalysis was funded by the U.S. Navy and the Modeling and Simulation Coordination Office. The HYCOM output is publicly available at https://www.hycom.org/dataserver/gofs-3pt0/reanalysis. The ERA5 reanalysis data can be obtained at https://www.ecmwf.int/en/forecasts/datasets/reanalysis-datasets/era5. The JTWC best-track data are from https://www.metoc.navy.mil/jtwc/jtwc.html website. The data analysis is supported by the High Performance Computing Division and HPC managers of Wei Zhou and Dandan Sui in the South China Sea Institute of Oceanology.

Data Availability

The data presented in this study are available on request from the author (juanli@scsio.ac.cn).

Appendix

More model-observation comparison

In order to further validate HYCOM near-inertial currents with more observations, three 75 KHz ADCPs moored at locations SCS1 (115.6°E, 18.1°N), SCS2 (115.0°E, 15.3°N), SCS3 (114.4°E, 13.0°N) are adopted for comparison (shown in Fig.1). The moored ADCPs are upward-looking with a bin size of 10 m and a sampling interval 1 h, which cover the period from 10 October 1998 to 10 January 1999. The near-inertial horizontal velocity profiles are derived from the raw ADCP velocities from -30 m to 200 m by using a band-pass filter with a frequency range of 0.85*f*-1.15*f*. The observed near-inertial currents and HYCOM near-inertial currents profiles during the observation period versus time at three sites are illustrated in Figs.S1. HYCOM near-inertial currents and observations display comparable magnitude and common variations on their vertical distributions with time, although there exist some discrepancies in SCS2. The correlation coefficients between the depth-integrated observed NIKE and HYCOM-simulated NIKE reach up to 0.60, 0.60 and 0.80, respectively.

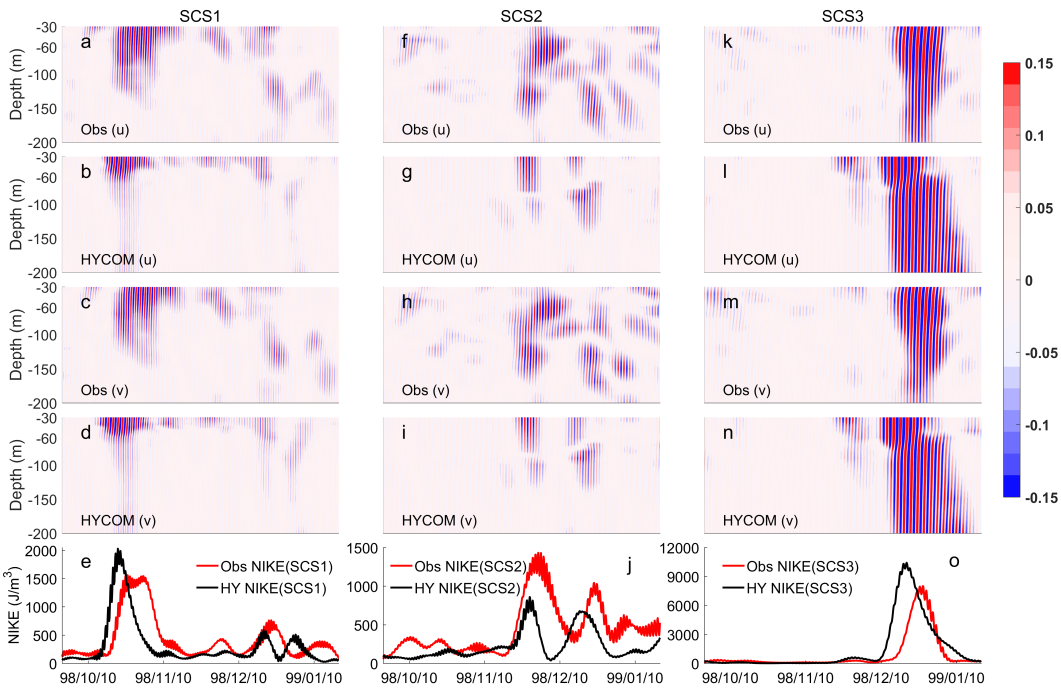

Fig. S1. Profiles of the eastward (a, f, k) and northward components (c, h, m) of observed near-inertial currents (m/s) and the eastward (b, g, l) and northward (d, i, n) components of HYCOM near-inertial currents versus time at locations SCS1, SCS2 and SCS3 from 10 October 1998 to 10 January 1999. (e, j, o) Depth-integrated obsevbed NIKE (red line, J/m^3) and HYCOM-simulated NIKE (black line) from -30 m to -200 m at locations SCS1, SCS2 and SCS3.

References

Abdillah, M. R. , Kanno, Y. , Iwasaki, T. , & Matsumoto, J. . (2021). Cold surge pathways in east asia and their tropical impacts. *Journal of Climate*, 34(1), 157-170.

Amante C, Eakins BW. (2009). ETOPO1 1 arc-minute global relief model: procedures, data sources and analysis. NOAA Technical Memorandum NESDIS NGDC-24, Boulder (Co).

Anderson, I., Huyer, A., & Smith, R. L. (1983). Near-inertial motions off the Oregon coast. *Journal of Geophysical Research: Oceans, 88*(C10), 5960-5972.

Alpers, W. , Wong, W. K. , Dagestad, K. F. , & Chan, P. W. . (2012). A northerly winter monsoon surge over the south china sea studied by remote sensing and a numerical model. *International Journal of Remote Sensing*, 33(23), 7361-7381.

Cao, A., Guo, Z., Pan, Y., Song, J., He, H., & Li, P. (2021). Near-inertial waves induced by Typhoon Megi (2010) in the South China Sea. *Journal of Marine Science and Engineering*, 9(4), 440.

Cao, A., Guo, Z., Song, J., Lv, X., He, H., & Fan, W. (2018). Near-Inertial Waves and Their Underlying Mechanisms Based on the South China Sea Internal Wave Experiment (2010-2011). *Journal of Geophysical Research: Oceans*, *123*(7), 5026-5040.

Chang, C. P. , Harr, P. A. , & Chen, H. J. . (2005). Synoptic disturbances over the equatorial south china sea and western maritime continent during boreal winter. *Monthly Weather Review*, 133(3), 489.

Chen, C., Reid, R. O., & Nowlin Jr, W. D. (1996). Near-inertial oscillations over the Texas-Louisiana shelf. *Journal of Geophysical Research: Oceans, 101*(C2), 3509-3524.

Chen, G., Xue, H., Wang, D., & Xie, Q. (2013). Observed near-inertial kinetic energy in the northwestern South China Sea. *Journal of Geophysical Research: Oceans*, *118*(10), 4965-4977.

Chen, S., Chen, D., & Xing, J. (2017). A study on some basic features of inertial oscillations and near-inertial internal waves. *Ocean Science, 13*(5), 829-836.

Chen, S., Hu, J., & Polton, J. A. (2015). Features of near-inertial motions observed on the northern south china sea shelf during the passage of two typhoons. *Acta Oceanologica Sinica, 34*(1), 38-43.

Chu, X., Chen, G., & Qi, Y.(2020). Periodic Mesoscale Eddies in the South China Sea. *Journal of Geophysical Research: Oceans*, 125, e2019JC015139.

Crawford, G. B., & Large, W. G. (1996). A numerical investigation of resonant inertial response of the ocean to wind forcing. *Journal of physical oceanography, 26(6)*, 873-891.

D'Asaro, E. A. (1985). The energy flux from the wind to near-inertial motions in the surface mixed layer. *Journal of Physical Oceanography*, *15*(8), 1043-1059.

Dickinson, M., & Molinari, J. (2002). Mixed Rossby-gravity waves and western Pacific tropical cyclogenesis. Part I: Synoptic evolution. *Journal of the Atmospheric* S*ciences, 59*(14), 2183-2196.

Ding, W., Liang, C., Liao, G., Li, J., Lin, F., Jin, W., & Zhu, L. (2018). Propagation characteristics of near-inertial waves along the continental shelf in the wake of the 2008 Typhoon Hagupit in the northern South China Sea. *Bulletin of Marine Science*, 94(4), 1293-1311.

Dippe, T., Zhai, X., Greatbatch, R. J., & Rath, W. (2015). Interannual variability of wind power input to near-inertial motions in the North Atlantic. *Ocean Dynamics*, *65*(6), 859-875.

Furuichi, N., Hibiya, T., & Niwa, Y. (2008). Model-predicted distribution of wind-induced internal wave energy in the world's oceans. *Journal of Geophysical Research*, *113*(C9), 597-606.

Gao, J., Wang, J., & Wang, F. (2019). Response of near-inertial shear to wind stress curl and sea level. *Scientific reports*, 9(1), 1-11.

Guan, S., Zhao, W., Huthnance, J., Tian, J., & Wang, J. (2014). Observed upper ocean response to typhoon Megi (2010) in the Northern South China Sea. *Journal of Geophysical Research: Oceans, 119*(5), 3134-3157.

He, Y., Cai, S., Wang, D., & He, J. (2015). A model study of Luzon cold eddies in the northern South China Sea. *Deep Sea Research Part I: Oceanographic Research*

Papers, *97*, 107-123.

Hisaki, Y., & Naruke, T. (2003). Horizontal variability of near-inertial oscillations associated with the passage of a typhoon. *Journal of Geophysical Research: Oceans, 108*(C12).

Hou, H., Yu, F., Nan, F., Yang, B., Guan, S., & Zhang, Y. (2019). Observation of near-inertial oscillations induced by energy transformation during typhoons. *Energies*, 12(1), 99.

Jarvis, J. R. (1995). Analysis of the East Asian Cold Surge Using a 15-Year Navy Data Set. NAVAL POSTGRADUATE SCHOOL MONTEREY CA.

Jiang, J., Lu, Y., & Perrie, W. (2005). Estimating the energy flux from the wind to ocean inertial motions: the sensitivity to surface wind fields. *Geophysical Research Letters*, *32*(15), 291-310.

Klein, P., Lapeyre, G., & Large, W. G. (2004). Wind ringing of the ocean in presence of mesoscale eddies. *Geophysical research letters, 31*(15).

Kung, H. S., & Gan, J. (2020). Response of near-inertial energy to a supercritical tropical cyclone and jet in the South China Sea: modelling study. *Ocean Science*, 16(5), 1095-1110.

Large, W. G. , & Pond, P. . (1981). Open ocean momentum flux measurements in moderate to strong winds. *Journal of Physical Oceanography*, 11(3), 324-336.

Le Boyer, A., Alford, M. H., Pinkel, R., Hennon, T. D., Yang, Y. J., Ko, D., & Nash, J. (2020). Frequency shift of near-inertial waves in the South China Sea. *Journal of Physical Oceanography*, 50(5), 1121-1135.

Li, T., & Wang, B. (2005). A review on the western North Pacific monsoon Synoptic-to-interannual variabilities. *Terr. Atmos. Oceanic Sci, 16*, 285-314.

Li, J., Liu, J., Cai, S., & Pan, J. (2015). The spatiotemporal variation of the wind-induced near-inertial energy flux in the mixed layer of the South China Sea. *Acta Oceanologica Sinica*, 34(1), 66-72.

Li, J., Xu, J., Liu, J., He, Y., Chen, Z., & Cai, S. (2019). Correlation of near-inertial wind stress in typhoon and typhoon-induced oceanic near-inertial kinetic energy in the upper South China Sea. *Atmosphere*, 10(7), 388.

Lian, Z., Fang, G., Wei, Z., Wang, G., Sun, B., & Zhu, Y. (2015). A comparison of wind stress datasets for the South China Sea. *Ocean Dynamics*, 65(5), 721-734.

Liu, J., He, Y., Li, J., Cai, S., Wang, D., & Huang, Y. (2018). Cases Study of Nonlinear Interaction Between Near-Inertial Waves Induced by Typhoon and Diurnal Tides Near the Xisha Islands. *Journal of Geophysical Research: Oceans, 123*(4), 2768-2784.

Monterey, G., and S. Levitus. (1997), Seasonal Variability of Mixed Layer Depth fo the World Ocean, NOAA Atlas NESDIS 14, 100 pp., Natl. Oceanic and Atmos. Admin., Silver Spring, Md.

Oey, L. Y. , Ezer, T. , Wang, D. P. , Fan, S. J. , & Yin, X. Q. . (2006). Loop current warming by hurricane wilma. *Geophysical Research Letters*, 33(8), 153-172.

Oey, L. Y. , & Chou, S. (2016). Evidence of rising and poleward shift of storm surge in western north pacific in recent decades. *Journal of Geophysical Research: Oceans, 121*(7), 5181-5192.

Pang, B. , & Lu, R. . (2019). Two distinct types of extratropical circulation anomalies associated with cold surges over the south china sea. *Journal of Climate*, 32(16).

Pollard, R. T. , & Millard, R. C. . (1970). Comparison between observed and simulated wind-generated inertial oscillations. *Deep Sea Research & Oceanographic Abstracts*, 17(4), 813,IN5,817-816,IN5,821.

Powell, M. D., Vickery, P. J., & Reinhold, T. A. (2003). Reduced drag coefficient for high wind speeds in tropical cyclones. *Nature*, 422(6929), 279-283.

Qu, T. (2000). Upper-layer circulation in the South China Sea. *Journal of Physical Oceanography*, *30*(6), 1450-1460.

Qu, T., Girton, J. B., & Whitehead, J. A. (2006). Deepwater overflow through Luzon strait. *Journal of Geophysical Research: Oceans, 111*(C1).

Rath, W., Greatbatch, R. J., & Zhai, X. (2014). On the spatial and temporal distribution of near-inertial energy in the Southern Ocean. *Journal of Geophysical Research: Oceans, 119*(1), 359-376.

Rimac, A., Storch, J. S., Eden, C., & Haak, H. (2013). The influence of high-resolution wind stress field on the power input to near-inertial motions in the ocean. *Geophysical Research Letters, 40*(18), 4882-4886.

Saha, S., et al. (2010). The NCEP climate forecast system reanalysis. *Bulletin of th American Meteorological Society*, *91*(8), 1015-1057.

Shu, Y., Pan, J., Wang, D., Chen, G., Sun, L., & Yao, J. (2016). Generation of near-inertial oscillations by summer monsoon onset over the South China Sea in 1998 and 1999. *Deep Sea Research Part I: Oceanographic Research Papers*, *118*, 10-19.

Sun, H., Yang, Q., Zhao, W., Liang, X., & Tian, J. (2016). Temporal variability of diapycnal mixing in the northern South China Sea. *Journal of Geophysical Research: Oceans, 121*(12), 8840-8848.

Sun, J., Oey, L. Y., Chang, R., Xu, F., & Huang, S. M. (2015). Ocean response to typhoon Nuri (2008) in western Pacific and South China Sea. *Ocean Dynamics*, 65(5), 735-749.

Sun, J., Oey, L., Xu, F. H., & Lin, Y. C. (2017). Sea level rise, surface warming, and the weakened buffering ability of South China Sea to strong typhoons in recent decades. *Scientific reports*, 7(1), 1-9.

Sun, L., Zheng, Q., Wang, D., Hu, J., Tai, C. K., & Sun, Z. (2011). A case study of near-inertial oscillation in the south china sea using mooring observations and satellite altimeter data. *Journal of Oceanography, 67*(6), 677-687.

Sun, Z., Hu, J., Zheng, Q., & Gan, J. (2015). Comparison of typhoon-induced near-inertial oscillations in shear flow in the northern South China Sea. *Acta Oceanologica Sinica, 34*(11), 38-45.

Takayabu, Y. N., & Nitta, T. (1993). 3-5 day-period disturbances coupled with convection over the tropical Pacific Ocean. *Journal of the Meteorological Society of Japan. Ser. II, 71*(2), 221-246.

Tangang, F. T., Juneng, L., Salimun, E., Vinayachandran, P. N., Seng, Y. K., Reason, C. J. C., ... & Yasunari, T. (2008). On the roles of the northeast cold surge, the Borneo vortex, the Madden-Julian Oscillation, and the Indian Ocean Dipole during the extreme 2006/2007 flood in southern Peninsular Malaysia.

Geophysical Research Letters, 35(14).

Thomas, L. N., & Zhai, X. (2022). The lifecycle of surface-generated near-inertial waves. In Ocean Mixing (pp. 95-115). Elsevier.

Wang, B., Huang, F., Wu, Z., Yang, J., Fu, X., & Kikuchi, K. (2009). Multi-scale climate variability of the South China Sea monsoon: A review. *Dynamics of Atmospheres and Oceans*, *47*(1-3), 15-37.

Wang, G., Su, J., Ding, Y., & Chen, D. (2007). Tropical cyclone genesis over the South China Sea. *Journal of Marine Systems, 68*(3-4), 318-326.

Waterhouse, A. F., MacKinnon, J. A., Nash, J. D., Alford, M. H., Kunze, E., Simmons, H. L., ... & Talley, L. D. (2014). Global patterns of diapycnal mixing from measurements of the turbulent dissipation rate. *Journal of Physical Oceanography, 44(7)*, 1854-1872.

Xiao, J., Xie, Q., Wang, D., Yang, L., Shu, Y., Liu, C., ... & Chen, G. (2016). On the near-inertial variations of meridional overturning circulation in the South China Sea. *Ocean Science, 12*(1), 335-344.

Xiao, X., Wang, D., Zhou, W., Zhang, Z., Qin, Y., He, N., & Zeng, L. (2013). Impacts of a wind stress and a buoyancy flux on the seasonal variation of mixing layer depth in the South China Sea. *Acta Oceanologica Sinica, 32*(9), 30-37.

Xu, Z., Yin, B., Hou, Y., & Xu, Y. (2013). Variability of internal tides and near-inertial waves on the continental slope of the northwestern South China Sea. *Journal of Geophysical Research-space Physics, 118*(1), 197-211.

Xu, Z., Liu, K., Yin, B., Zhao, Z., Wang, Y., & Li, Q. (2016). Long-range propagation and associated variability of internal tides in the South China Sea. *Journal of Geophysical Research: Oceans*, 121(11), 8268-8286.

Yang, B., Hu, P., & Hou, Y. (2021). Observed Near-Inertial Waves in the Northern South China Sea. *Remote Sensing*, 13(16), 3223.

Yang, L., Wang, D., Huang, J., Wang, X., Zeng, L., Shi, R., ... & Yuan, J. (2015). Toward a mesoscale hydrological and marine meteorological observation network in the South China Sea. *Bulletin of the American Meteorological Society, 96*(7), 1117-1135.

Yang, Y., HSU, P., & He, J. (2016). Energetic characteristics of multi-scale interaction in the strong and weak years of south china sea summer monsoon. *Acta Meteorologica Sinica, 74*(4), 556-571.

Zeng, L., Li, X., Du, Y., Shi, R., Yao, J., Wang, D., & Sui, D. (2012). Synoptic-scale disturbances over the northern South China Sea and their responses to El Niño. *Acta Oceanologica Sinica*, 31(5), 69-78.

Zeng, L., Wang, Q., Xie, Q., Shi, P., Yang, L., Shu, Y., ... & Wang, D. (2015). Hydrographic field investigations in the Northern South China Sea by open cruises during 2004-2013. *Science Bulletin, 60*(6), 607-615.

Zhai, X. (2015). Latitudinal dependence of wind-induced near-inertial energy. *Journal of Physical Oceanography, 45*(12), 3025-3032.

Zhai, X. (2017). Dependence of energy flux from the wind to surface inertial currents on the scale of atmospheric motions. *Journal of Physical Oceanography, 47*(11), 2711-2719.

Zhai, X., Greatbatch, R. J., Eden, C., & Hibiya, T. (2009). On the loss of wind-induced near-inertial energy to turbulent mixing in the upper ocean. *Journal of Physical Oceanography*, *39*(11), 3040-3045.

Zhang, H. , He, H. , Zhang, W. Z. , & Tian, D.. (2021). Upper ocean response to tropical cyclones: a review. *Geoscience Letters*, 8, 1.

Zhou, X., Zhang, Y., Yang, Y., Yang, Y., & Han, S. (2013). Evaluation of anomaliesin GLDAS-1996 dataset. *Water Science and Technology*, *67*(8), 1718-1727.

Zhou, C., Zhao, W., Tian, J., Yang, Q., & Qu, T. (2014). Variability of the deep-water overflow in the Luzon Strait. *Journal of Physical Oceanography, 44*(11), 2972-2986.